Ab initio calculations on low-lying electronic states of TeO_2 and Franck-Condon simulation of the $(1)^1B_2 \leftarrow \tilde{X}^1A_1$ TeO_2 absorption spectrum including anharmonicity

Edmond P. F. Lee,[a] Daniel K. W. Mok,[a),b)] and Foo-tim Chau
Department of Applied Biology and Chemical Technology, Hong Kong Polytechnic University, Hung Hom, Hong Kong

John M. Dyke
Department of Chemistry, University of Southampton, Highfield, Southampton SO17 1BJ, United Kingdom

(Received 30 March 2004; accepted 12 May 2004)

Ab initio calculations have been carried out on low-lying singlet and triplet states of TeO_2 at different levels of theory with basis sets of up to the augmented-polarized valence-quintuple-ζ quality. Equilibrium geometrical parameters, harmonic vibrational frequencies, and relative electronic energies of the $\tilde{X}\,^1A_1$, $^1B_1$, $^1B_2$, $^1A_2$, $^3A_1$, $^3B_1$, $^3B_2$, and $^3A_2$ states of TeO_2 have been calculated. Potential energy functions (PEFs) of the $\tilde{X}\,^1A_1$ and the $(1)^1B_2$ states were computed at the complete-active-space self-consistent-field multireference configuration interaction level, with a basis set of augmented-polarized valence-quadruple-ζ quality. Franck-Condon factors (FCFs) for the electronic transition between the $\tilde{X}\,^1A_1$ and $(1)^1B_2$ states of TeO_2 were calculated with the above-mentioned *ab initio* PEFs. The $(1)^1B_2 \leftarrow \tilde{X}\,^1A_1$ absorption spectrum of TeO_2 was simulated employing the computed FCFs, which include Duschinsky rotation and anharmonicity, and compared with the recently published laser-induced fluorescence (LIF) spectrum of Hullah and Brown [J. Mol. Spectrosc. **200**, 261 (2000)]. The *ab initio* results and spectral simulation reported here confirm the upper electronic state involved in the LIF spectrum to be the $(1)^1B_2$ state of TeO_2 and also confirm the vibrational assignments of Hullah and Brown. However, our simulated spectrum suggests that the reported LIF spectrum from 345 to 406 nm represents only a portion of the full $(1)^1B_2 \leftarrow \tilde{X}\,^1A_1$ absorption spectrum of TeO_2, which extends from ca. 406 to 300 nm. Another dye other than the two used by Hullah and Brown is required to cover the 345–300 nm region of the LIF band. *Ab initio* calculations show strong configuration mixing of the $(1)^1B_2$ electronic surface with higher $^1B_2$ states in a region of large TeO bond length ($\geqslant$2.0 Å) and OTeO bond angle ($\geqslant$135.0°). © *2004 American Institute of Physics.* [DOI: 10.1063/1.1768164]

I. INTRODUCTION

Recently, Hullah and Brown[1] reported the jet-cooled laser-induced fluorescence (LIF) excitation spectrum of TeO_2 in the 345–406 nm region, where TeO_2 was prepared in the gas phase for spectroscopic study by heating the solid dioxide to 1123 K under ca. 2.5 bar of argon and expanding the vapor through a ca. 250 μm hole. The observed electronic transition was assigned very tentatively to the $^1B_2 \leftarrow \tilde{X}\,^1A_1$ transition of TeO_2 based on comparison with the $^1B_2$-$\tilde{X}\,^1A_1$ system[2] of SeO_2 observed at ca. 320 nm. Although there have been a significant number of *ab initio* investigations on the $\tilde{X}\,^1A_1$ state of TeO_2,[3–8] only one of them[6] also studied the low-lying singlet and triplet excited states of TeO_2. In Ref. 6, results of complete-active-space self-consistent field (CASSCF) calculations were reported on the lowest $^1A_1$, $^1B_1$, $^1B_2$, $^1A_2$, $^3A_1$, $^3B_1$, $^3B_2$, and $^3A_2$ states of TeO_2, employing the CEP-31G* and RCEP-41G* basis sets for O and Te, respectively. Bending potential energy curves of these electronic states were reported, and their equilibrium geometrical parameters were obtained. The vertical (T_{vert}) and adiabatic (T_e) electronic excitation energies of the excited states from the $\tilde{X}\,^1A_1$ state were calculated. The computed T_{vert} and T_e values of the $^1B_2$ state from Ref. 6 are 4.04 and 3.50 eV, respectively (note that in Ref. 6, because a different axis system was employed, the irreducible representations of B_1 and B_2 in the C_{2V} point group are interchanged as compared to these ones used here). However, the identified (0-0) band in the LIF spectrum of Ref. 1 was measured to be at 25 423 cm^{-1} (=3.152 eV), and a fitted ν_0 value of 25 526 cm^{-1} (=3.165 eV) was obtained from the vibrational progressions observed in the LIF spectrum. The *ab initio* T_e value from Ref. 6 is larger than these experimental T_0 values by ca. 0.35 eV. In addition, the reported LIF band[1] appears to have two maxima at ca. 25 852 cm^{-1} (3.205 eV; 386.7 nm) and 27 421 cm^{-1} (3.400 eV; 364.7 nm), with the highest observed band position of the LIF spectrum being at ca. 345 nm (3.594 eV; 28 986 cm^{-1}). The observed band maxima are lower in energy than the calculated T_{vert} value by more than 0.6 eV. In fact, the CASSCF T_{vert} is ca. 0.45 eV higher

[a)]Author to whom correspondence should be addressed. Electronic mail: epl@soton.ac.uk
[b)]Electronic mail: bcdaniel@polyu.edu.hk

TABLE I. Basis sets used in this work.

ECP	Te	O	Number of basis
A	Lanl2-[6*s*6*p*3*d*1*f*][a]	6-311+G (3*df*)	124
B	ECP46MWB-cc-pVQZ(no *g*)	cc-pVQZ(no *g*)	137
C	ECP46MWB-aug-cc-pVQZ(no *g*)	Aug-cc-pVQZ(no *g*)	185
D	ECP46MWB-aug-cc-pVQZ	Aug-cc-pVQZ	239
E	ECP46MWB-AV5Z[a]	Aug-cc-pV5Z	384
All electron (uncontracted)			
F	(18*s*14*p*9*d*) DZVP[b]	(10*s*6*p*1*d*) DZVP2[b]	185
G	(21*s*17*p*13*d*5*f*)[a]	(13*s*7*p*4*d*) aug-cc-pVQZ (*spd* only)	280

[a]Designed in this work; see text for details.
[b]From Ref. 20.

in energy than the position at which the LIF band in Ref. 1 decreases to zero intensity. Clearly, the agreement of the *ab initio* T_{vert} and T_e values with the positions of the observed band maxima and the fitted ν_0 value {and/or the measured (0-0) band position}, respectively, cannot be considered as good. It appears that the only available *ab initio* calculations on the excited states of TeO_2 of Ref. 6 do not provide unambiguous support for the assignment of the upper electronic state involved in the LIF spectrum to the $^1B_2$ state of TeO_2, as suggested in Ref. 1. Nevertheless, the basis sets used in Ref. 6 are small, and the CASSCF method employed therein lacks dynamic electron correlation. In view of these shortcomings in the calculations carried out in Ref. 6, we propose to carry out near state-of-the-art *ab initio* calculations on the low-lying electronic states of TeO_2 in order to clarify the assignment of the upper electronic state of the LIF band reported in Ref. 1. In addition, we also propose to carry out Franck-Condon simulation of the $^1B_2 \leftarrow \tilde{\mathbf{X}}\,^1A_1$ absorption spectrum of TeO_2 in order to obtain fingerprint-type identification of the observed LIF spectrum, as we have done previously for the chemiluminescence spectrum of HPCl,[9] the SVL emission spectra of AlNC,[10] the LIF spectrum of GaN_2,[11] and the SVL emission spectra of PO_2.[12]

II. THEORETICAL CONSIDERATIONS AND COMPUTATIONAL DETAILS

A. *Ab initio* calculations: general

Geometry optimization, harmonic vibrational frequency, and relative electronic energy calculations were carried out on a large number of low-lying electronic states of TeO_2 employing the CIS, CASSCF, B3LYP, MP2, QCISD, CCSD(T), and CASSCF multireference configuration interaction (MRCI) methods. The basis sets used in the present study are summarized in Table I. Since Te is a rather heavy element, two effective core potentials (ECPs) namely, LANL2DZ (Ref. 13) and ECP46MWB,[14] were used, both accounting for 46 core electrons of Te, leaving the valence $5s^25p^4$ electrons to be described by the valence basis set. The ECP46MWB-aug-cc-pVQZ basis set of Te is the standard (16*s*12*p*4*d*3*f*2*g*)/[5*s*5*p*4*d*3*f*2*g*] basis set designed for Te to be used with the ECP46MWB ECP by Martin and Sundermann.[15] Both the standard ECP46MWB-aug-cc-pVQZ basis set and its slightly modified variants were used, as shown in Table I, together with basis sets of O of corresponding qualities.[16] The lanl2-[6*s*6*p*3*d*1*f*] and ECP46MWB-AV5Z basis sets for Te (see Table I) were designed as follows.

The lanl2-[6*s*6*p*3*d*1*f*] basis set used has the contraction coefficients of the contracted [1*s*] and [1*p*] functions obtained from an ROHF calculation of atomic Te employing the LANL2DZ ECP and an uncontracted (17*s*17*p*) even-tempered primitive set (both the *s* and *p* sets have a ratio of exponents of 1.5, and tightest *s* and *p* exponents of 25.628 907 and 17.085 938, respectively). The contracted [1*s*1*p*] set was augmented with uncontracted 5*s* (ratio =2.5; tightest exponent=2.0), 5*p* (2.5; 1.25), 3*d* (4.0; 1.2), and 1*f* (exponent=0.2) functions to give the [6*s*6*p*3*d*1*f*] contraction. The lanl2-[6*s*6*p*3*d*1*f*] basis set of Te was used with the 6-311+G (3*df*) basis set of O (denoted as basis *A* for TeO_2; see Table I). Basis *A* was used in geometry optimization and/or harmonic vibrational frequency calculations, employing the GAUSSIAN (Ref. 17) suite of program.

The ECP46MWB-AV5Z basis set of Te has the contraction coefficients of the contracted [1*s*] and [1*p*] functions obtained from an ROHF calculation of atomic Te employing the ECP46MWB ECP and an uncontracted (23*s*19*p*) even-tempered primitive set (both the *s* and *p* sets have a ratio of 1.5, and center *s* and *p* exponents of 4.0 and 1.0, respectively). The contracted [1*s*1*p*] set was augmented with uncontracted 6*s* (ratio=2.5; tightest exponent=4.0), 6*p* (2.5; 3.0), 5*d* (3.0; 3.6), 4*f* (3.5; 2.14375), 3*g* (4.0; 0.84), and 2*h* (4.0; 0.22) functions to give the [7*s*7*p*5*d*4*f*3*g*2*h*] contraction, which is slightly larger than the standard aug-cc-pV5Z basis set. The ECP46MWB-AV5Z basis set of Te was used with the standard aug-cc-pV5Z basis set[18] of O (denoted as basis *E* for TeO_2; see Table I). Basis *E* is the largest basis set used in the present study, with the total number of basis functions of 384, and was used in both geometry optimization and single energy calculations, employing the MOLPRO (Ref. 19) suite of program.

The GAUSSIAN (Ref. 17) suite of programs was employed to carry out the CIS, B3LYP, MP2, QCISD, and CCSD(T) geometry optimization and harmonic frequency calculations. Unrestricted-spin UHF wave functions were used with GAUSSIAN for open-shell singlet and triplet states, except in the CIS calculations (UHF—unrestricted Hartree-Fock). Spin contamination is small for the triplet states studied (computed $\langle S^2 \rangle$ values of less than 2.13), though the calculated $\langle S^2 \rangle$ values for the open-shell singlet states are

larger than 1.0, as expected. Nevertheless, spin-projected energies are used at the MP2 level for all open-shell states. The MOLPRO (Ref. 19) suite of programs was employed to perform CASSCF, CASSCF/MRCI, and RCCSD(T) geometry optimization and/or single energy calculations. Only the O $1s^2$ electrons were frozen in these calculations (with the core electrons of Te being accounted for by the ECP employed). A full valence active space has been used in most of the CASSCF calculations, except in some averaged state calculations involving a large number of states. In the latter cases, it was found that a larger than full valence active space was required for the CASSCF calculations to achieve convergence. With basis *D* (augment-polarized quadruple-ζ quality), the numbers of uncontracted and contracted configurations in the internally contracted MRCI calculations are over 1×10^9 and 4×10^6, respectively, for the singlet states and over 2×10^9 and 6.4×10^6 for the triplet states. With basis *E* (augment-polarized quintuple-ζ quality), the numbers of uncontracted and contracted configurations in the internally contracted MRCI calculations are ca. 3×10^9 and 7.7×10^6, respectively, for the singlet states. It should be noted that the MRCI energies quoted throughout the present work have included the Davidson correction.

In addition, relativistic contributions were calculated for the $\tilde{\mathbf{X}}\,^1A_1$ and $(1)^3B_2$ states of TeO_2 (see later text) using MOLPRO by two different methods. First, the expectation values of the mass-velocity and Darwin terms were calculated employing the Cowan-Griffin operator with the Hartree-Fock wave function. Second, relativistic SCF calculations were carried out employing the Douglas-Kroll (DK) relativistic one-electron integrals. The relativistic contribution was taken as the difference between the total energies obtained from the relativistic SCF calculation and nonrelativistic Hartree-Fock (HF) calculation, $[E_{rel}(DK)-E_{non\text{-}rel}(HF)]$, employing the same basis set. Two uncontracted all-electron basis sets were employed in these relativistic calculations to assess basis set effects. First, the uncontracted all-electron DZVP-DFT-orb and DZVP2-DFT-orb basis sets[20] were used for Te and O, respectively, giving a total number of basis functions of 185 (denoted as basis *F*; see Table I). Second, an uncontracted even-tempered $(21s17p13d5f)$ set was used for Te: $21s$ (ratio=2.5; center exponent=100.0), $17p$ (2.5; 30.0), $13d$ (2.5; 7.0), and $5f$ (3.75; 1.5), and the uncontracted $(13s7p4d)$ set from the aug-cc-pVQZ (spd only) basis set[16,18] was used for O, giving a total number of basis functions of 280 (denoted as basis *G*). The uncontracted $(15s9p5d)$ set of the aug-cc-pV5Z (spd only) basis set for O was also used together with the $(21s17p13d5f)$ basis set of Te, but they gave essentially identical results as with the $(13s7p4d)$ set of the aug-cc-pVQZ (spd only) basis set for O. This is expected, as the relativistic contribution from O is significantly smaller than that from Te, which is significantly heavier than O.

The general strategy used in this work is described briefly as follows. Since a large number of electronic states were considered, we started with the simplest CIS level. The CASSCF, MP2, QCISD, and CCSD(T) methods were then employed with the smaller basis sets given in Table I. Finally the RCCSD(T) and CASSCF/MRCI methods with larger basis sets were employed. The lowest singlet and triplet states of each irreducible representation in the C_{2V} point group were first investigated. Some higher states were also considered at the CASSCF level, as discussed in the following section. One main aim of the present investigation is to obtain reliable computed T_e and T_{vert} values of the low-lying electronic states of TeO_2, in order to ascertain the assignment of the upper electronic state involved in the observed LIF spectrum of Ref. 1. In this connection, various levels of calculations, in terms of electron correlation and basis size, were carried out as described, and the trends in the calculated minimum-energy geometrical parameters, harmonic vibrational frequencies, and/or relative electronic energies were examined to assess the reliability of the computed quantities. As will be discussed in the following section, the only candidate, which fits the upper state of the LIF spectrum, in terms of calculated T_e values, is the $(1)^1B_2$ state, with the open-shell electronic configuration of $(a_2)^1(b_1)^1$ (obtained on excitation of an electron from the doubly occupied valence a_2 molecular orbital to the lowest unoccupied b_1 molecular orbital; see the following section). Therefore, energy points on the electronic energy surfaces of the $\tilde{\mathbf{X}}\,^1A_1$ and $(1)^1B_2$ states were computed, followed by variational calculations of anharmonic vibrational wave functions of both electronic states. Then Franck-Condon factor (FCF) calculations were carried out between the $(1)^1B_2$ and $\tilde{\mathbf{X}}\,^1A_1$ states of TeO_2, as described in the following section.

B. CASSCF/MRCI potential energy functions and anharmonic vibrational wave functions of the $\tilde{\mathbf{X}}\,^1A_1$ and $(1)^1B_2$ states of TeO_2, and Franck-Condon simulation of the $(1)^1B_2\leftarrow\tilde{\mathbf{X}}\,^1A_1$ absorption spectrum of TeO_2

For each electronic state studied, the potential energy function (PEF) *V* was determined by fitting the following polynomial to an appropriate number of CASSCF/MRCI/D (aug-cc-pVQZ quality) single-point energies.

$$V=\sum_{ij} C_{ij}(S_1)^i(S_2)^j+V_{eqm}. \tag{1}$$

The PEF is expressed as displacements of symmetry coordinates, $S_1=(\Delta r_1+\Delta r_2)/\sqrt{2}$, and the bending coordinates suggested by Carter and Handy,[21] $S_2=\Delta\theta+\alpha\Delta\theta^2+\beta\Delta\theta^3$, where $\Delta r_{1,2}$ and $\Delta\theta$ are displacements in the r(TeO) bond lengths (for the symmetric stretch, $\Delta r_1=\Delta r_2$) and θ(OTeO) bond angle from the corresponding equilibrium values, respectively.

For the $\tilde{\mathbf{X}}\,^1A_1$ state of TeO_2, 76 CASSCF/MRCI/D energy points covering the ranges of $r=1.43-2.13$ Å and $\theta=90°-140°$ were computed. For the $(1)^1B_2$ state, 143 energy points covering the ranges of $r=1.39-2.30$ Å and $\theta=60°-145°$ were calculated. The nonlinear least-squares fit procedure,[22] NL2SOL, was employed to obtain the C_{ij}'s, V_{eqm}, r_{eqm}, θ_{eqm}, α, and β from the computed single-point energy data. The asymmetric stretching mode has not been considered, because the observed bands in the LIF spectrum do not show any identifiable vibrational structure associated with the asymmetric stretching mode.[1]

Variational calculations, which employed the rovibronic Hamiltonian for a nonlinear molecule of Watson,[23] were carried out to obtain the anharmonic vibrational wave functions. The latter were expressed as linear combinations of harmonic oscillator functions, $h(v_1,v_2)$, where v_1 and v_2 denote the quantum numbers of the harmonic basis functions for the symmetric stretching and bending mode, respectively (see Ref. 24 for details). Harmonic basis functions, up to $h(10,10)$ with a restriction of $v_1+v_2<10$, were employed in the variational calculation of the $\tilde{\mathbf{X}}\,^1A_1$ state of TeO_2. For the $(1)^1B_2$ state, the upper state of the $^1B_2\leftarrow\tilde{\mathbf{X}}\,^1A_1$ transition which shows dominant structure in both the stretching and the bending modes in the LIF band, harmonic basis functions of up to $h(20,20)$ with a restriction of $v_1+v_2<20$ were used. A larger harmonic basis set of up to $h(30,30)$, with a restriction of $v_1+v_2<30$, has also been used, but the energies of the vibrational states obtained are essentially identical to those obtained using a smaller harmonic basis set.

FCFs were computed employing the anharmonic vibrational wave functions and allowing for Duschinsky rotation, as described previously (see Ref. 25 and references therein). The iterative-Franck-Condon-analysis (IFCA) procedure, where the geometry change on excitation was varied slightly around the best *ab initio* computed geometry change upon excitation, while the geometrical parameters of the $\tilde{\mathbf{X}}\,^1A_1$ state of TeO_2 were fixed at the *ab initio* value (see later text), was carried out to obtain the best match between the simulated and experimental spectra. A Gaussian function with a full width at half maximum of 7 cm^{-1} (ca. 0.1 nm in the 375 nm region) was used for the simulated band for each vibrational component. The relative intensity of each vibrational component in a simulated absorption spectrum is given by the corresponding computed anharmonic FCF and a frequency factor of power 1.

III. RESULTS AND DISCUSSION

A. *Ab initio* calculations

The *ab initio* results are summarized in Tables I–V. It is noted that the numbering of the molecular orbitals used in the electronic configurations described in the present study is for the valence molecular orbitals, excluding the O 1*s* frozen core orbitals (the lowest a_1 and b_2 molecular orbitals) for the sake of simplicity. For the $\tilde{\mathbf{X}}\,^1A_1$ state, the valence electronic configuration is $\cdots(4a_1)^2(1b_1)^2(3b_2)^2(1a_2)^2$, excluding the lowest a_1 and b_2 O 1*s* orbitals (note also that the order of the orbitals presented does not imply energy order).

1. Optimized geometrical parameters

First, the optimized geometrical parameters of the $\tilde{\mathbf{X}}\,^1A_1$ state obtained at different levels of calculation are considered. From Table II, it can be seen that both basis size and electron correlation effects affect the calculated equilibrium geometrical parameters. Nevertheless, the computed bond angles θ_e show convergence with larger basis sets and higher levels of electron correlation. It can be concluded that the best theoretical bond angle of the $\tilde{\mathbf{X}}\,^1A_1$ state of TeO_2 has a value of $111.2\pm0.3°$. Regarding the computed bond lengths r_e, however, they do not appear to be converging with basis size, though the CCSD(T) and CASSCF/MRCI values obtained with the same basis sets are very consistent. Nevertheless, the spread of the computed r_e values obtained using the larger basis sets *D* and *E* is ca. 0.010 Å., and we can quote the best theoretical estimate of r_e of 1.780 ± 0.005 Å for the $\tilde{\mathbf{X}}\,^1A_1$ state of TeO_2. Previous calculations on the $\tilde{\mathbf{X}}\,^1A_1$ state of TeO_2 as shown in Table II are largely at significantly lower levels of theory in terms of basis set size and electron correlation than those of the present study and hence can be considered as less reliable. The available experimentally derived geometrical parameters of the $\tilde{\mathbf{X}}\,^1A_1$ state of TeO_2 have large uncertainties (see Table II). Nevertheless, comparing the experimental and theoretical values, the agreement in θ_e is reasonably good, though the available experimental r_e values appear to be too large.

For the lowest $^1B_1$, $^1B_2$, and $^1A_2$ states of TeO_2, the trends in the computed θ_e and r_e values with levels of calculation (see Table III) are generally similar to those of the $\tilde{\mathbf{X}}\,^1A_1$ state discussed above, except that the variations of θ_e with theory, particularly in terms of level of electron correlation, are larger for the low-lying excited open-shell singlet states than for the $\tilde{\mathbf{X}}\,^1A_1$ state. The most extreme example is for the $(1)^1B_1$ state. The computed θ_e values of this state range between 107.1° and 131.2° (Table III), with a wide spread of 24.1°. For these open-shell singlet states, wave functions obtained with UHF based methods (e.g., UMP2) have large spin contamination and wave functions obtained with the restricted-spin multireference methods (CASSCF and CASSCF/MRCI) should be more reliable. In addition, it is also clear that basis set size effects are also important for obtaining reliable equilibrium geometrical parameters of these open-shell singlet states. The computed r_e values of all three open-shell singlet states obtained at the CASSCF level from Ref. 6, using the relatively small RECP-41G* and ECP-31G* basis sets for Te and O, respectively, are larger than the corresponding values obtained in the present study by ca. 0.1 Å. The computed θ_e values from Ref. 6 also differ significantly from those obtained in the present work. For instance, θ_e was calculated to be 108.0° for the $(1)^1B_2$ state at the CASSCF/RECP-41G*;ECP-31G* level from Ref. 6, but to be 101.88 (99.23)° at the CASSCF/B (CASSCF/MRCI/E) levels in the present study. It is evident that the basis sets used here are considerably larger than those used in Ref. 6, and the results obtained here particularly at the CASSCF/MRCI level, which include both dynamic and nondynamic electron correlations, should be more reliable. For the $(1)^1B_2$ state, the basis set *E*, which is of the aug-cc-pV5Z quality, was also employed to obtain the minimum-energy geometry at the CASSCF/MRCI level. The differences in the computed r_e and θ_e values between employing the basis sets *D* (aug-cc-pVQZ quality) and *E* (aug-cc-pV5Z quality) are 0.010 Å and 0.23°, respectively, indicating that the computed θ_e values are converging readily with basis size, while the computed r_e value with the basis sets *D* or *E* has an uncertainty of ca. ±0.005 Å, similar to that obtained for the $\tilde{\mathbf{X}}\,^1A_1$ state, discussed above.

The computed geometrical parameters obtained in this work and in Ref. 6 for the low-lying triplet states of TeO_2 are

TABLE II. Optimized geometrical parameters and calculated harmonic vibrational frequencies (in cm^{-1}) of the $\tilde{X}\,^1A_1$ state of TeO_2 obtained at different levels of calculation and available corresponding experimental values.

Method[a]	R_e (Å)	θ_e (deg)	$\omega_1(a_1)$	$\omega_2(a_1)$	$\omega_3(a_2)$
B3LYP/A	1.7769	112.45	858.8	286.1	872.6
MP2/A	1.7986	113.34	802.2	269.2	838.9
QCISD/A	1.7726	112.87	849.2	291.0	864.7
CCSD(T)/A	1.7865	113.05	814.3	278.1	836.9
CAS/B	1.7897	110.98			
CCSD(T)/D	1.7836	111.57			
CAS/MRCI/D	1.7851	111.41			
CAS/MRCI/D PEF	1.7851	111.36	856.3	288.3	
(fundamental frequencies)			(851.1)	(287.7)	
CCSD(T)/E	1.7736	111.15			
CASSCF/MRCI/E	1.7749	111.01			
HF/[10*s*8*p*5*d*];[4*s*2*p*][b]	1.801	111.6			
HF/ECP[5*s*5*p*2*d*];[4*s*2*p*][b]	1.790	112.9			
HF/ECP[6*s*5*p*3*d*];[4*s*4*p*][c]	1.767	113.6			
HF/ECP-31G(*d*,*d*′)[d]	1.77	113.0			
CAS/RCEP-41G*;CEP-31G*[,e]	1.83	111.9			
MP2/ECP(211/2111/1);6-311+G*[,f]	1.843	112.4	786	255	843
CCSD(T)/ECP(211/2111/1);6-311+G*[,f]	1.837	112.0			
MP2/RECP[41+G2*d*];RECP[31G*d*][f]	1.8350	114.2	787	253	831
CISD+Q/RECP[41+G2*d*];RECP[31G*d*][g]	1.8054	113.5	833	277	858
ED[h]	1.83±2				
IR/matrix (Ar, isotopic frequencies)[i]	1.9	110±2			
IR/matrix (Kr; ν)[j]				289.2	
IR/matrix (Ar; ν)[i]			822.6		839.4
IR/matrix (Ne; ν)[i]			826.4		844.8
IR (estimated gas ν)[i]			830±3	270±30	849±3
IR/matrix (N_2; ν)[k]			831.7	294	848.3
IR/gas; ν^f				279	853
LIF[l]			823	282	
(fundamental frequencies)			(824.7)	(281.1)	

[a]See Table I and text for the basis sets used in the present study. All correlated calculations carried out in the present study have the O 1*s* electrons frozen, except the B3LYP calculations.
[b]Reference 3.
[c]Reference 4.
[d]Reference 5.
[e]Reference 6.
[f]Reference 7.
[g]Reference 8.
[h]Electron diffraction; Ref. 26.
[i]Reference 27.
[j]Reference 28.
[k]Reference 29.
[l]Reference 1.

shown in Table III. It has been noted above that, for the triplet states studied here [see later text for the $(1)^3A_1$ state], spin contamination is negligibly small with UHF based methods. The trends of the computed results obtained for the triplet states are in general similar to those of the corresponding excited singlet states discussed, suggesting that spin contamination is indeed not an influential factor in both cases. Summarizing, it has been shown that both basis set size and electron correlation effects are important in determining reliable equilibrium geometrical parameters of low-lying singlet and triplet states of TeO_2. The *ab initio* calculations carried out in the present study are significantly superior to, and hence the results obtained are more reliable than, those reported previously. Lastly, when the geometrical change upon excitation from the $\tilde{X}\,^1A_1$ state to the $(1)^1B_2$ state is considered, the changes in r_e and θ_e are $+0.0935$ Å and $-12.02°$, respectively, at the CASSCF/MRCI level with the basis set *D* (aug-cc-pVQZ quality) and $+0.0935$ Å and $-11.78°$ at the CASSCF/MRCI level with the basis set *E* (aug-cc-pV5Z quality). These *ab initio* geometry changes are very consistent and would not be expected to change significantly with any further improvement in the level of calculation in terms of basis set size and valence electron correlation. The equilibrium geometrical parameters of the $(1)^1B_2$ state will be further discussed, when the simulated absorption spectra are compared with the experimental LIF spectrum,[1] and the IFCA geometry of the $(1)^1B_2$ state is considered.

2. Calculated harmonic and fundamental vibrational frequencies

Since a large amount of experimental data and some theoretical data are available on the vibrational frequencies

TABLE III. Computed minimum-energy geometrical parameters, harmonic vibrational frequencies (cm^{-1}), and relative electronic energies (T_e, with respect to the $\tilde{X}\,^1A_1$ state) of some lowest singlet and triplet states of TeO_2 obtained at different levels of calculations.[a]

$(1)^1B_1(4a_1)^1(2b_1)^1$	r_e (Å)	θ_e (deg)	$\omega_1(a_1)$	$\omega_2(a_1)$	$\omega_3(a_2)$	T_e (eV) (cm^{-1})
CIS (nstates=15)/A	1.7804	114.27	861.5	262.4	736.0	···
UMP2/A	1.8034	131.22	824.4	198.9	1748.2	1.915 (15 445)
UQCISD/A	1.8516	113.60	696.8	220.7	563.9	2.133 (17 206)
UCCSD(T)/A	1.8532	115.84				2.310 (18 630)
CAS/B	1.8754	109.01				2.510 (20 244)
CAS/MRCI/D	1.8597	111.01				2.484 (20 038)
CAS/RECP-41G*,[b]	1.95	107.1				2.34
$(1)^1B_2(1a_2)^1(2b_1)^1$						
CIS (nstates=15)/A	1.8087	100.44	845.1	270.2	450.8	···
UMP2/A	1.8755	108.40	763.4	196.9	501.0	3.077 (24 814)
UQCISD/A	1.8516	113.60	684.8	238.5	466.4	2.547 (20 547)
UCCSD(T)/A	1.8832	100.66				2.504 (20 198)
CAS/B	1.8927	101.88				3.667 (29 577)
CAS/MRCI/D	1.8788	99.46				3.395 (27 384)
CAS/MRCI/D PEF	1.8786	99.35	709.2	224.9		
(fundamental freq.)			(702.7)	(224.7)		
CAS/MRCI/E	1.8684	99.23				3.715 (29 962)
CAS/RECP-41G*,[b]	1.97	108.0				3.50
LIF (0-0)			679	220		3.152 (25 423)
(fundamental freq.)			(672.7)	(215.0)		
$(1)^1A_2(3b_2)^1(2b_1)^1$						
CIS (nstates=15)/A	1.7858	95.12	910.8	260.2	795.6	···
UMP2/A	1.8305	78.31	868.4	310.9	1269.5	1.644 (13 260)
UQCISD/A	1.8568	88.13	733.1	218.8	633.0	1.876 (15 132)
UCCSD(T)/A	1.8620	87.20				2.060 (16 615)
CAS/B	1.8709	91.40				2.256 (18 197)
CAS/MRCI/D	1.8549	88.22				2.156 (17 393)
CAS/RECP-41G*,[b]	1.94	92.0				2.10
$(1)^3A_1\cdots(b_1)^1(b_1)^1$						
CIS (nroot=6)/A	1.8401	106.57	807.3	294.9	967.6	···
UMP2/A(=>$^3A_2$)						
CAS/B	1.9242	110.02				4.171 (33 639)
RCCSD(T)/D	1.9011	108.16				3.981 (32 109)
CAS/MRCI/D	1.9090	108.38				3.922 (31 632)
CAS/RCEP41G*,[b]	1.94	180.0				2.92
$(1)^3B_1\cdots(a_1)^1(b_1)^1$						
CIS (nroot=2)/A	1.7602	121.04	872.2	247.9	843.7	···
UMP2/A	1.8022	134.66	827.5	200.9	1526.1	2.608 (21 033)
CAS/B	1.8566	114.23				2.206 (17 792)
RCCSD(T)/D	1.8325	117.75				2.152 (17 357)
CAS/MRCI/D	1.8396	116.86				2.128 (17 162)
CAS/RCEP41G*,[b]	1.93	113.0				2.11
$(1)^3B_2\cdots(a_2)^1(b_1)^1$						
CIS (root=1)/A	1.8139	100.40	876.6	301.8	724.1	···
UMP2/A	1.8660	100.09	696.4	254.9	193.6	3.258 (26 277)
CAS/B	1.8887	100.97				1.857 (14 899)
RCCSD(T)/D	1.8708	100.24				2.061 (16 622)
CAS/MRCI/D	1.8732	100.68				2.019 (16 282)
CAS/RCEP41G*,[b]	1.95	102.1				1.64
$(1)^3A_2\cdots(b_2)^1(b_1)^1$						
CIS (root=3)/A	1.7884	95.16	907.9	259.6	835.6	···
UMP2/A	1.8359	79.08	845.9	296.4	1164.5	2.583 (20 831)
CAS/B	1.8693	90.80				2.109 (17 013)
RCCSD(T)/D	1.8486	86.75				2.016 (16 262)
CAS/MRCI/D	1.8531	87.96				1.997 (16 107)
CAS/RCEP41G*,[b]	1.93	91.8				1.96

[a]See Table I for the basis sets *A*, *B*, *C*, *D*, and *E*. All calculations are from the present investigation, except the CAS/RCEP41G* calculations (see footnote b).

[b]From Ref. 6; note that the irreducible representations B_1 and B_2 used there are interchanged cf. here, because of the different axis systems used.

TABLE IV. Calculated excitation energies [T_e and T_{vert} in eV (cm^{-1})] from the $\tilde{X}\,^1A_1$ state to three low-lying excited states of TeO_2 obtained at different levels[a] of theory.

T_{vert}	$(1)^1B_1$	$(1)^1B_2$	$(1)^1A_2$
CIS (nstates=15)/A[b]	3.148(25 392)	4.514 (36 410)	3.604(29 067)
[CIS/A: Oscillator strengths, f]	[0.0124]	[0.0529]	[0.0]
CAS(averaged state)/C[b,c]	2.338(18 859)	3.984 (32 132)	2.398(19 340)
CAS/C: Dipole matrix elements	−0.244 (x)	0.873 (y)	0.0
CAS/C[b]	2.817(22 722)	4.167 (33 606)	2.859(23 056)
CAS/MRCI/C[b]	2.692(21 713)	3.881 (31 301)	2.790(22 503)
CAS/D[d]	2.769(22 336)	4.089 (32 984)	2.778(22 407)
CAS/MRCI/D[d]	2.660(21 453)	3.811 (30 737)	2.717(21 912)
CAS/E[d]	2.587(20 864)	3.898 (31 440)	2.598(20 958)
CAS/MRCI/E[d]	2.668(21 516)	3.808 (30 710)	2.768(22 325)
CAS/RCEP-41G*; CEP-31G*[,e]	2.71	4.04	2.66
T_e			
UMP2/A	1.915(15 445)	3.077 (24 814)	1.644(13 260)
UQCISD/A	2.133(17 206)	2.547 (20 547)	1.876(15 132)
UCCSD(T)/A	2.310(18 630)	2.504 (20 198)	2.060(16 615)
CAS/B	2.510(20 244)	3.667 (29 577)	2.256(18 197)
CAS/D	2.545(20 524)	3.672 (29 616)	2.283(18 414)
CAS/MRCI/D	2.484(20 038)	3.395 (27 384)	2.156(17 393)
CAS/E//CASSCF/MRCI/D	2.583(20 829)	3.709 (29 919)	2.319(18 701)
CAS/MRCI/E//CASSCF/MRCI/D	2.541(20 495)	3.450 (27 827)	2.210(17 828)
CAS/E//CASSCF/MRCI/E		3.715 (29 962)	
CAS/MRCI/E		3.452 (27 839)	
ΔE_{rel}(CG)[f]/uncontracted DZVP (est.[g])		−0.169 (−1365)	
ΔE_{rel}(DK)[h]/uncontracted DZVP (est.[g])		−0.189 (−1459)	
ΔE_{rel}(CG)[f]/(21s17p13d5f) (est.[g])		−0.133 (−1074)	
ΔE_{rel}(DK)[h]/(21s17p13d5f) (est.[g])		−0.144 (−1160)	
Estimated relativistic contributuion (ave.)		−0.160 (−1265)	
ΔZPE (QCISD/A)		−0.038 (−307)	
Best estimated theoretical T_0[i]		3.257 (26267)	
CAS/RCEP-41G*; CEP-31G*[,e]	2.34	3.50	2.10
Absorption[j]		3.176 (25618)	
LIF (observed 0-0 band)		3.152 (25423)	
LIF (fitted ν_0)		3.165 (25526)	

[a]See text for details of the basis sets used in the present study.

[b]At the B3LYP/A geometry of the $\tilde{X}\,^1A_1$ state of T_eO_2.

[c]In order to achieve convergence in the CASSCF calculation, an active space of full valence plus one more b_1 and one more a_2 virtual molecular orbital are required.

[d]At the CASSCF/MRCI/D geometry of the $\tilde{X}\,^1A_1$ state.

[e]From Ref. 6; note that the irreducible representations B_1 and B_2 used there are interchanged cf. here, because of the different axis systems used.

[f]The expectation values of the mass-velocity and Darwin terms were calculated employing the Cowan-Griffin operator, as implemented in MOLPRO.

[g]The difference of the calculated relativistic contributions between the $\tilde{X}\,^1A_1$ and $^3B_2$ states was used to estimate that between the $\tilde{X}\,^1A_1$ and $^1B_2$ states; see text.

[h]The relativistic SCF calculations were carried out employing the Douglas-Kroll relativistic one-electron integrals, as implemented in MOLPRO. The relativistic contribution was taken as the difference between the total energies obtained from the nonrelativistic Hartree-Fock calculation and relativistic SCF calculation, $[E_{rel}(DK)-E_{nonrel}(HF)]$, employing the same basis set; see text.

[i]The CAS/MRCI/E relative electronic energy plus the averaged relativistic contribution and the zero-point vibrational energy correction (ΔZPE).

[j]References 30 and 31.

of the $\tilde{X}\,^1A_1$ state of TeO_2, as shown in Table II, the $\tilde{X}\,^1A_1$ state is considered first. The respective computed MP2 and CCSD(T) harmonic vibrational frequencies of all three modes obtained in the present study with the basis set *A* are close to each other and are smaller than the corresponding QCISD values. The smaller QCISD values are most likely due to the lack of triple excitations in the QCISD method, which with the CCSD(T) method have brought the calculated quantities back close to those obtained at the MP2 level. The B3LYP values are close to the QCISD ones and also to those obtained at the CASSCF/MRCI level, but the CASSCF/MRCI calculations have employed a significantly larger basis set *D* (aug-cc-pVQZ quality). Summing up, similar to the computed equilibrium geometrical parameters discussed above, both basis size and electron correlation effects are affecting the calculated vibrational frequencies. The CASSCF/MRCI/D level is currently the highest level used to calculate the vibrational frequencies of the $\tilde{X}\,^1A_1$ state of

TABLE V. Calculated vertical excitation electronic energies (eV) of the low-lying singlet and triplet states of TeO_2 from the $\tilde{\mathbf{X}}\,^1A_1$ state at different levels of theory.[a]

T_{vert}	Config.[b]	CIS/A	CAS/C[c]	CAS/C[d]	MRCI/D	CCSD(T)/D	MRCI/E	CAS[e]
$(1)^3B_1$	$(4a_1)^1(2b_1)^1$	2.07	1.86	2.53	2.25	2.27		2.37
$(1)^3B_2$	$(2b_1)^1(1a_2)^1$	1.80	2.33	2.03	2.40	2.45		2.14
$(1)^3A_2$	$(2b_1)^1(3b_2)^1$	3.07	2.18	2.48	2.55	2.61		2.52
$(1)^1B_1$	$(4a_1)^1(2b_1)^1$	3.16	2.34	2.63	2.66		2.67	2.71
$(1)^1A_2$	$(2b_1)^1(3b_2)^1$	3.58	2.35	2.60	2.72		2.77	2.66
$(1)^1B_2$	$(2b_1)^1(1a_2)^1$	4.50	3.97	3.89	3.81		3.81	4.04
$(1)^3A_1$	$(1b_1)^1(2b_1)^1$	3.85	4.51	4.71	4.50	4.45		4.52
$(2)^3A_2$	$(2b_1)^1(2b_2)^1(3b_2)^2$			4.99				
$(2)^1A_2$	$(2b_1)^1(2b_2)^1(3b_2)^2$			5.02				
$(2)^3B_1$	$(3a_1)^1(4a_1)^2(2b_1)^1$			5.02				
$(2)^1B_1$	$(3a_1)^1(4a_1)^2(2b_1)^1$			5.21				
$(2)^3B_2$	$(4a_1)^1(2b_1)^2(3b_2)^1$			5.34				
$(2)^1A_1$	$(2b_1)^2(1a_2)^0$			5.66[f]				
$(2)^3A_1$	$(4a_1)^1(5a_1)^1$			6.07				
$(2)^1B_2$	$(4a_1)^1(2b_1)^2(3b_2)^1$			6.64				

[a]At CASSCF/MRCI/E geometry of the $\tilde{\mathbf{X}}\,^1A_1$ state; MRCI refers to CASSCF/MRCI calculations.

[b]The major electronic configurations of the open shells are given. The numberings of the molecular orbitals are for the valence molecular orbitals, excluding the O 1*s* frozen core orbitals (the lowest a_1 and b_2 molecular orbitals). The $\tilde{\mathbf{X}}\,^1A_1$ state has the electronic configuration of $\ldots\ldots(4a_1)^2(1b_1)^2(3b_2)^2(1a_2)^2$.

[c]Averaged states (eight states) with an active space of full valence plus two more vacant molecular orbitals of b_1 and a_2 symmetries (see text).

[d]Three states averaged state CASSCF calculations (full valence active): The $\tilde{\mathbf{X}}\,^1A_1$ state and the two lowest states of each spin symmetry, giving the relative energies of the two states with respect to the $\tilde{\mathbf{X}}\,^1A_1$ state.

[e]From Ref. 6; the RCEP-41G* and CEP-31G* basis sets were used for Te and O, respectively. Note that the irreducible representations B_1 and B_2 used there are interchanged cf. here, because of the different axis systems used.

[f]Two states CASSCF, giving the $\tilde{\mathbf{X}}\,^1A_1$ and $(2)^1A_1$ states.

TeO_2 (from the PEF). Both the harmonic and fundamental frequencies of the symmetric stretching and bending modes were obtained at this level of calculation, and the differences between the computed harmonic and fundamental frequencies are small ($<6\ cm^{-1}$), suggesting small anharmonic effects. The spread and the average of calculated ω_2 values of the $\tilde{\mathbf{X}}\,^1A_1$ state using the basis set *A* at different levels are ca. 22 and 281.1 cm^{-1}, respectively. The ω_2 and ν_2 values obtained from the PEF at the CASSCF/MRCI level with the basis set *D* are 288.3 and 287.7 cm^{-1}, respectively. These theoretical ω_2 and ν_2 values agree very well with the available experimental ν_2 values from IR matrix studies and the gas phase LIF ω_2 and ν_2 values of 282 and 281.1 cm^{-1}. Previously computed ω_2 values are mostly smaller than the corresponding available experimental values. Regarding ω_1, the spread of the computed values obtained at different levels from the present study is ca. 57 cm^{-1}, which is rather large. The difference between the CCSD(T)/A and CASSCF/MRCI/D ω_1 values is 42 cm^{-1}, which is also quite large, suggesting that the shape of the energy surface in the symmetric stretching coordinate is rather dependent on the levels of theory and the basis sets used. Nevertheless, the CASSCF/MRCI/D υ_1 value agrees reasonably well with the experimental value obtained from the hot band of the LIF spectrum (to within 26 cm^{-1}). The agreement between the calculated ν_3 values and the experimental values, mostly from infrared matrix isolation studies, is also reasonably good (to within 20 cm^{-1}; see Table II).

No theoretical values are available for the vibrational frequencies of any excited state of TeO_2 prior to the present study, and no experimental vibrational frequencies are available for other electronic states of TeO_2, except for the $\tilde{\mathbf{X}}\,^1A_1$, as discussed, and for the $(1)^1B_2$ states from the LIF study of Ref. 1. From Tables II and III, it is clear that the computed vibrational frequencies of all the electronic states of TeO_2 studied are highly dependent on the levels of calculations used to obtain them. For the $(1)^1B_2$ state of TeO_2, both the experimental fundamental and harmonic vibrational frequencies of the symmetric stretching and bending modes have been reported in Ref. 1. The calculated ν_2 and ω_2 values agree very well with the corresponding experimental values, particularly with the CASSCF/MRCI/D values from the *ab initio* PEF (to within 10 cm^{-1}; see Table III). The agreement between the CASSCF/MRCI/D and experimental ν_1 and ω_1 values is ca. 30 cm^{-1}. Based on the above comparisons, it could be concluded that computed *ab initio* vibrational frequencies obtained from the present investigation largely support the vibrational assignments of the LIF bands given in Ref. 1.

3. Calculated excitation energies of low-lying singlet and triplet states of TeO_2

From Tables III–V, where the computed T_{vert} and/or T_e values obtained in the present study are summarized, it is clear that relative electronic energies are very dependent on the levels of calculation and their reliable evaluation demands very high levels of theory. Nevertheless, the T_e values of all the triplet and singlet states of TeO_2 reported here are obtained up to the RCCSD(T) and/or CASSCF/MRCI levels of theory and with basis set *D*, which is of aug-cc-pVQZ quality (Tables IV and V). Comparing the computed T_e values of the low-lying singlet and triplet states of TeO_2 obtained at the highest levels of calculation shown in Tables III

and IV [i.e., RCCSD(T) or CASSCF/MRCI with basis sets *D* or *E*; ignoring relativistic contributions for the time being] with available experimental T_0 values (Table IV), the computed T_e value of the $(1)^1B_2$ state agrees best with the experimental T_0 value. The calculated T_e values of all other excited singlet and triplet states of TeO_2 agree poorly with the experimental T_0 value given by Hullah and Brown.[1]

From the major electronic configurations and the corresponding calculated configuration interaction (CI) coefficients of the low-lying singlet states of TeO_2 obtained at the CASSCF/MRCI/D level, the $(1)^1B_2$ state is formed from the $\tilde{\mathbf{X}}\,^1A_1$ state when an electron is excited from the doubly occupied $1a_2$ molecular orbital to the lowest unoccupied $2b_1$ molecular orbital. The computed CASSCF and RHF wave functions of the $(1)^1B_2$ state reveal that the $1a_2$ molecular orbital is a purely O_2 localized orbital (O_2 $2p_x$ out-of-plane antibonding π_g combination) with no contribution from Te valence $5s$ and $5p$ orbitals by symmetry, while the $2b_1$ molecular orbital is essentially an out-of-plane Te $5p_x$ and O_2 $2p_x$ (π_u) antibonding combination, with a larger contribution from the Te $5p_x$ out-of-plane orbital than the O_2 $2p_x$ (π_u) orbitals. The computed charge densities on Te, based on the Mulliken population analysis, for the $\tilde{\mathbf{X}}\,^1A_1$ and $(1)^1B_2$ states of TeO_2 are ca. $+2.0$ and $+1.67$, respectively, suggesting a significant electron density transfer from O_2 to Te upon excitation. In view of the different electronic configurations, computed molecular wave functions and charge densities of the $\tilde{\mathbf{X}}\,^1A_1$ and $(1)^1B_2$ state of TeO_2, the question of the adequacy of employing the same quasirelativistic ECP, ECP46MWB, for these two electronic states of TeO_2, in terms of relativistic contributions, is raised. Consequently, relativistic calculations as described above employing the all-electron basis sets *F* and *G* (Table I) were carried out to investigate the different relativistic contributions of the two states and their effects on the computed T_e value. However, because MOLPRO is unable to perform both relativistic and nonrelativistic ROHF calculations on an open-shell singlet state, the corresponding $(1)^3B_2$ state with the same electronic configuration as the $(1)^1B_2$ state was studied instead, and the computed relativistic contribution of the triplet state was used as an estimate for that of the corresponding singlet state. Table IV gives the differences between the relativistic contributions to the computed electronic energies of the $\tilde{\mathbf{X}}\,^1A_1$ and $(1)^3B_2$ states obtained by two different methods and two basis sets. The average of the differences obtained at different levels of calculation is -0.16 eV, which is not trivial. The negative sign means that the relativistic contribution to the total electronic energy of the $(1)^1B_2$ state is larger than that of the $\tilde{\mathbf{X}}\,^1A_1$ state, as expected from the consideration of the electronic configurations, the compositions of the occupied molecular orbitals, and computed charge densities of the two states. We simply take this averaged value of -0.16 eV obtained for the $(1)^3B_2$ state to approximate the relativistic effect on the T_e value of the $(1)^1B_2$ state. The best estimated theoretical T_0 value of the $(1)^1B_2$ state, including this relativistic correction, is 3.257 eV (see Table IV), which agrees with the experimental T_0 value to within 0.1 eV. In view of the approximation involved in estimating the relativistic contribution to the theoretical T_e value of the $(1)^1B_2$ state, this agreement between theory and experiment can be considered as satisfactory. Summing up, the best *ab initio* T_0 value supports strongly the assignment of the upper electronic state associated with the observed spectral band in the LIF (Ref. 1) and absorption (Refs. 30 and 31) spectra to the $(1)^1B_2$ state of TeO_2.

Considering T_{vert}, the computed value of the $(1)^1B_2$ state at the highest level of calculation is 3.81 ± 0.01 eV (325.4 nm; 30 730 cm^{-1}), which is ca. 0.36 eV (2872 cm^{-1}) above the T_e value obtained at the same level calculation. If the experimental (0-0) position of 3.152 eV is taken as the reference point, this *ab initio* T_{vert}/T_e energy difference yields a T_{vert} value of ca. 3.51 eV (28 295 cm^{-1}; 353 nm), which is near the energy position at which the experimental LIF band[1] drops to zero intensity on the high energy side. Although the details of the intensity distribution of the vibrational envelope of a spectral band depend on the FCFs of the vibrational components involved, which will be discussed later, the comparison of the computed T_{vert} value with the observed LIF spectrum suggests a significant loss of spectral intensity in the LIF spectrum in the T_{vert} region. One possible cause for the loss of spectral intensity is due to predissociation arising from a nearby repulsive electronic state through an avoided crossing. In order to investigate this possibility, the vertical excitation energies of both the first and second excited singlet and triplet states of each irreducible representation in the C_{2V} point group were calculated at the CASSCF/C level and the results are summarized in Table V (see footnotes *d* and *f* for the details of the calculations). First, comparing the computed T_{vert} values obtained at different levels of theory for all the first excited singlet and triplet states of all four irreducible representations in the C_{2V} point group, it can be concluded that the CASSCF/C level of calculation is reasonably reliable. From Table V, it is clear that in the vertical excitation region, there is no electronic state, which is close to the $(1)^1B_2$ state. The nearest state is the $(1)^3A_1$ state, which is at least ca. 0.7 eV higher in energy in the vertical excitation region. Therefore, it can be concluded that the apparent disagreement between theory and experiment with respect to the *ab initio* T_{vert} value being significantly higher in energy than the observed band maxima, and being on the high energy side of the LIF band, is not due to interaction with a nearby state. This discrepancy between theory and experiment will be further investigated when the simulated absorption spectrum is compared with the LIF spectrum of Ref. 1.

B. The CASSCF/MRCI PEFs and anharmonic vibrational wave functions of the $\tilde{\mathbf{X}}\,^1A_1$ and $(1)^1B_2$ states of TeO_2

The CASSCF/MRCI/D PEFs of the $\tilde{\mathbf{X}}\,^1A_1$ and $(1)^1B_2$ states of TeO_2 are given in Table VI. The root mean square deviations of the fitted potentials from the computed single point energies are 7.7 and 9.7 cm^{-1} for the CASSCF/MRCI/D PEFs of the $\tilde{\mathbf{X}}\,^1A_1$ and $(1)^1B_2$ states, respectively. First, although the main electronic configurations of these two states are clear, their CI coefficients are less than 0.9.

TABLE VI. The CASSCF/MRCI PEFs of the $\tilde{X}\,^1A_1$ and $^1B_2$ states of TeO_2 (see text).

C_{ij}	$\tilde{X}\,^1A_1$	$(1)^1B_2$
20	0.7332	0.4870
11	−0.0072	−0.0287
2	0.1241	0.0877
30	−1.0370	−0.6549
21	0.0160	0.0134
12	−0.1934	−0.1763
3	0.0080	0.0044
40	0.8831	0.5585
31	0.1069	0.1411
22	0.0543	0.0187
13	−0.0013	−0.0217
4	0.0067	0.0413
50	0.0402	0.0091
5	0.0514	0.0336
60	−0.6243	−0.3775
6	0.3396	0.1920
41	⋯	−0.0586
32	⋯	−0.0835
23	⋯	−0.0105
14	⋯	−0.1240
07	⋯	−0.0232
08	⋯	−0.0645
70	⋯	−0.0828
78	⋯	0.0508
51	⋯	0.0226
42	⋯	−0.0167
33	⋯	−0.0149
24	⋯	0.0644
15	⋯	−0.0596
r_e	1.7851	1.8788
θ_e	1.9437	1.7354
α	−0.1016	0.0315

Some of the relatively large computed CI coefficients suggest nontrivial CI mixing even in the region of the equilibrium geometry of both states, particularly for the $(1)^1B_2$ state. In addition, the calculated T_1 diagnostic of the $\tilde{X}\,^1A_1$ state at its equilibrium geometry obtained from the RCCSD(T) calculation is 0.0305, which is also slightly large, suggesting nontrivial multireference character. Consequently, it was decided to calculate the $\tilde{X}\,^1A_1$ state PEF employing the CASSCF/MRCI method rather than the RCCSD(T) method. Second, the sum of the squares of the CI coefficients of the reference configurations in the MRCI calculation, Σc_{ref}^2, of all the energy points employed for the PEFs of both states are larger than 0.94, indicating that the reference space employed in these CASSCF/MRCI calculations is adequate and hence the calculated MRCI energies should be reliable. However, it should be pointed out that for three geometries with large r and large θ combinations (i.e., 1.95 Å and 145.0°, 2.3 Å and 105.0°, and 2.02 Å and 135.0°), CASSCF/MRCI calculations experienced CASSCF convergence failure. The corresponding MRCI wave functions suggest that contributions from other $^1B_2$ states become significant at these geometries. These $^1B_2$ states include the $^1B_2$ configuration with the two open shells $\cdots(4a_1)^2(5a_1)^1(3b_2)^1$ and also some low-spin singlet configurations with four open shells. Nevertheless, energy points at these three geometries, which have CASSCF convergence failures, have been excluded from the fitting of the PEF. It is estimated that, at these geometries in the large r/θ region of the $(1)^1B_2$ electronic energy surface, mixing from higher $^1B_2$ states begins to occur at energies larger than ca. 0.6 eV (5000 cm^{-1}) above the minimum. Combining with the experimental T_0 of 25 423 cm^{-1} from Ref. 1, the mixing of higher $^1B_2$ states is expected at excitation energies of larger than ca. 3.77 eV (30 400 cm^{-1}; 329 nm), which are near the high energy tail of the simulated absorption spectrum (see the following section) and outside the spectral range of the observed LIF spectrum of Ref. 1. It should also be noted that the mixing of higher $^1B_2$ states is significant only at these three geometries. For regions with larger r/θ and hence higher energies, the $(1)^1B_2$ state becomes dominant again.

From the computed coefficients of the harmonic basis functions in the anharmonic vibrational wave functions, it can be seen that the anharmonic effect is small, except for the bending mode of the $(1)^1B_2$ state. Also, mode mixing appears to be negligibly small. However, it should be noted that the $(n,m,0)$ vibrational levels of the $(1)^1B_2$ state are calculated to have energies higher than the $(n-1,m+3,0)$ vibrational levels by ca. 30–40 cm^{-1}, giving "doublet-type" vibrational structure in the simulated absorption spectrum, which will be discussed in the following section.

C. Simulated $(1)^1B_2 \leftarrow \tilde{X}\,^1A_1$ absorption spectra of TeO_2 and comparison with the experimental LIF spectrum of Hullah and Brown

Some simulated $(1)^1B_2 \leftarrow \tilde{X}\,^1A_1$ absorption spectra of TeO_2 are shown in Figs. 1–3. The experimental (0-0) band position of 25 423 cm^{-1} from Hullah and Brown[1] has been used for the position of the $(1)^1B_2(0,0,0) \leftarrow \tilde{X}\,^1A_1(0,0,0)$ vibrational component in all the simulated spectra presented here for the sake of easy comparison with the experimental LIF spectrum.[1] Since the available experimentally derived equilibrium geometrical parameters of the $\tilde{X}\,^1A_1$ state have large uncertainties, as discussed, all the simulated spectra shown have employed the equilibrium geometrical parameters of the $\tilde{X}\,^1A_1$ state obtained from the *ab initio* PEF. The IFCA procedure carried out led to an IFCA θ_e value of 100.1° for the $(1)^1B_2$ state and an IFCA r_e value, which is essentially the same as the *ab initio* value from the PEF. The IFCA bond angle change upon excitation is −11.26°, while the CASSCF/MRCI/D bond angle change is −12.02° from the PEFs. It has been mentioned above that the CASSCF/MRCI/E bond angle change upon excitation is −11.78°. Comparison between the calculated bond angle change upon excitation obtained employing basis sets *D* and *E* suggests a smaller bond angle change with a larger basis set. In this connection, the slightly smaller IFCA bond angle change upon excitation, compared to the *ab initio* values, is in line with the theoretical trend. Therefore, it is concluded that the agreement between the IFCA and highest level *ab initio* bond angle change upon excitation from the $\tilde{X}\,^1A_1$ state to the $(1)^1B_2$ state of TeO_2 is reasonably good. It is noted here that in the IFCA procedure, the matching between the simulated absorption and observed LIF spectra was focused mainly on

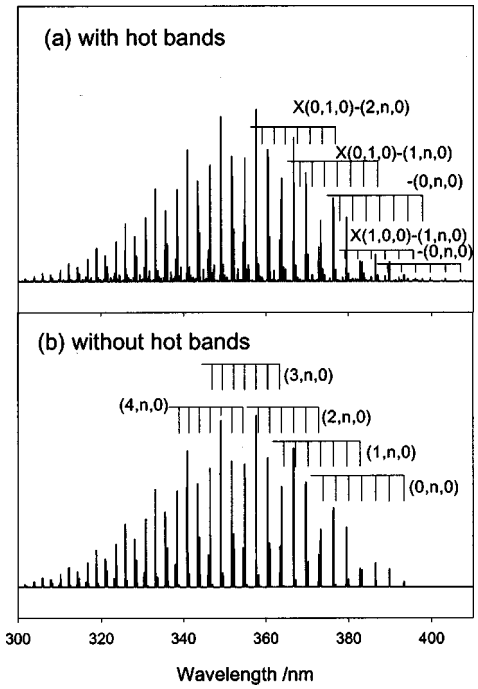

FIG. 1. Simulated $(1)^1B_2 \leftarrow \tilde{\mathbf{X}}\,^1A_1$ absorption spectra of TeO_2: The *ab initio* geometry of the $\tilde{\mathbf{X}}\,^1A_1$ state from the PEF (see Table II), and the r_e of 1.8786 Å (from *ab initio* PEF; see Table III) and the IFCA θ_e of 100.1° for the $^1B_2$ state were employed. The top trace (a) is with hot bands and the bottom trace (b) is without hot bands. The populations of the low-lying vibrational levels of the $\tilde{\mathbf{X}}\,^1A_1$ state of TeO_2 used to produce trace (a) are given in Table VII (see also text).

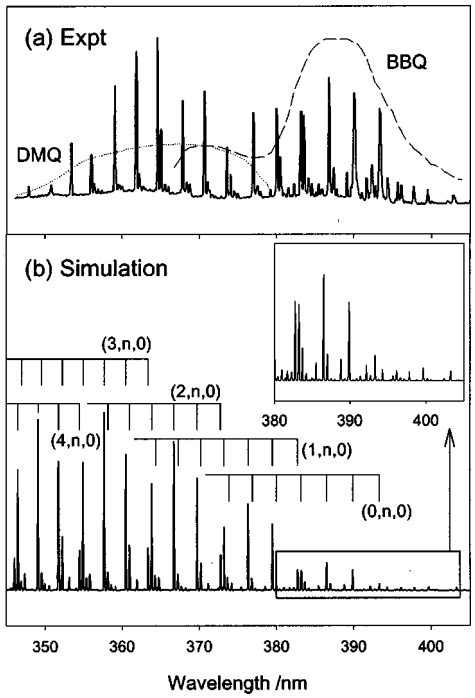

FIG. 2. The experimental LIF spectrum from Ref. 1 with the dye laser intensity curves [dots and broken lines for the DMQ and BBQ dyes, respectively; top trace (a)], and part of the simulated $(1)^1B_2 \leftarrow \tilde{\mathbf{X}}\,^1A_1$ absorption spectrum of TeO_2 [bottom trace (b); part of Fig. 1(a)]. The insert in (b), an expanded part of the simulated spectrum, is for clearer comparison with the LIF spectrum in the low excitation energy region of 380–405 nm (see also Fig. 3). The assignments of the main vibrational progressions in the upper state arising from excitation from the (0,0,0) vibrational level of the $\tilde{\mathbf{X}}\,^1A_1$ state are given in Fig. 2(b). See Fig. 3 for the vibrational designations of the hot bands.

the major vibrational structure and in the low excitation energy region (370–400 nm), with particular emphasis on the relative intensities of the $(1)^1B_2$ $(n,m,0)$ and $(n-1,m+3,0)$ doublet structure (see later text).

Figure 1(b) is a full simulated absorption spectra arising from excitation from the (0,0,0) vibrational level of the $\tilde{\mathbf{X}}\,^1A_1$ state; i.e., without hot bands. Figure 1(a) is a full simulated absorption spectrum with hot bands arising from a non-Boltzmann distribution for the vibrational population of the $\tilde{\mathbf{X}}\,^1A_1$ state. The non-Boltzmann distribution, which gives the simulated absorption spectrum that matches best with the low excitation energy region of the LIF spectrum, has the relative populations of the low-lying vibrational levels of the $\tilde{\mathbf{X}}\,^1A_1$ state given in Table VII. This population distribution is almost the same as a Boltzmann distribution at 200 K, except for the populations of the (1,0,0) and (1,1,0) levels of the $\tilde{\mathbf{X}}\,^1A_1$ state, which are ca. 15 and 20 times larger than those of a Boltzmann distribution at 200 K, respectively. These full simulated absorption spectra shown in Fig. 1 cover a spectral range from ca. 405 to 300 nm, with the $(1)^1B_2(3,2,0) \leftarrow \tilde{\mathbf{X}}\,^1A_1(0,0,0)$ vibrational component being the most intense component at an excitation energy of ca. 3.47 eV (357.5 nm), corresponding to the measured band position of 27 847 cm^{-1} (3.45 eV; 359 nm) in the LIF spectrum. The position of the simulated band maximum based on calculated Franck-Condon factors agrees very well with *ab initio* T_{vert} values discussed above, but it is near the high energy tail of the observed LIF spectrum,[1] where the observed vibrational intensity goes to zero [see also Fig. 2(a)]. Before this discrepancy between theory and experiment is discussed further, it should be noted, from the simulated spectrum shown in Fig. 1(b), which does not include hot bands, that the doublet structure of the $(1)^1B_2(n,m,0)$ and $(n-1,m+3,0)$ components is evident throughout the whole absorption band, in line with their computed energy separations of ca. 35 cm^{-1} discussed above. We will come back to this feature of the simulated $(1)^1B_2 \leftarrow \tilde{\mathbf{X}}\,^1A_1$ absorption spectrum, which is very important in providing fingerprint-type identification and confirmation of the vibrational assignments of the LIF spectrum.

Figure 2 shows the experimental LIF spectrum of Ref. 1 [Fig. 2(a)] and the portion of the simulated absorption spectrum in the same energy range of the LIF spectrum [Fig. 2(b); part of Fig. 1(a)] for comparison. The inset in Fig. 2(b) is an expanded version of the long wavelength (low excitation energy) region of the simulated absorption spectrum. In Fig. 2(a), the approximate gain curves of the two dyes, DMQ and BBQ, used in Ref. 1, as obtained from the manual of the manufacturer, are also shown. In Ref. 1, there is no mention of correction of the published LIF spectrum for the laser dye intensities. It is therefore assumed that no such correction has been made. Comparing the LIF spectrum with the two dye intensity curves as shown in Fig. 2(a), it seems clear that the intensity of the vibrational envelope of the LIF spectrum

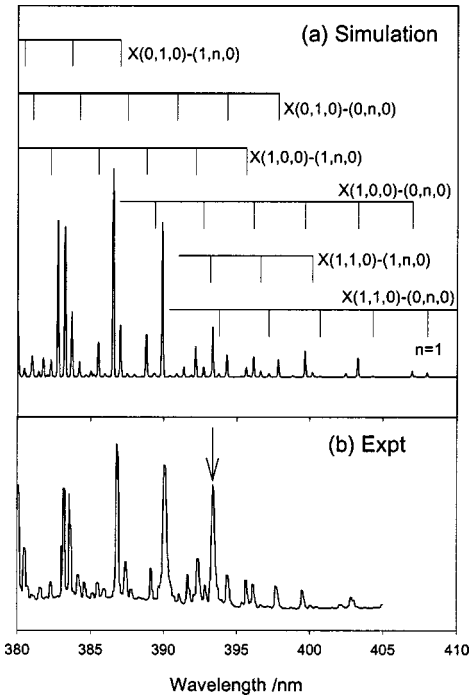

FIG. 3. The comparison between the simulated $(1)^1B_2 \leftarrow \tilde{\mathbf{X}}\,^1A_1$ absorption spectrum of TeO_2 and the observed LIF spectrum of Ref. 1 in the 380–410 nm region, with the vibrational designations of the hot bands (see also text). The arrow in the LIF spectrum indicates the (0-0) band position from Ref. 1.

follows very closely the two dye intensity curves. This is expected, but the comparison also suggests that the observed relative intensities of the vibrational components in the LIF spectrum appear to reflect mainly the dye laser intensities, which mask the true Franck-Condon factors of the vibrational components. If this conclusion is valid, there are at least two implications. First, the decrease to zero intensity of the LIF spectrum at 345 nm may simply be due to the decrease of the DMQ dye laser intensity and will not indicate the high energy end of the LIF spectrum. In this connection, an alternative dye to cover the higher energy region than those used in Ref. 1 will be required to investigate the higher excitation energy region ($<$345 nm) of the $(1)^1B_2 \leftarrow \tilde{\mathbf{X}}\,^1A_1$ TeO_2 LIF spectrum and to reveal the full extent of the spectrum and the position of the band maximum. The second implication is that a direct match between the observed LIF spectrum reported in Ref. 1, without correction of dye intensities, and the simulated absorption spectrum reported here, based on computed Franck-Condon factors, is understandably not very meaningful. Specifically, the observed two maxima in the LIF spectrum mentioned above are almost certainly due to the maxima of the two laser dye intensity curves and it is not a true reflection of the Franck-Condon factors. Nevertheless, comparing the LIF spectrum of Ref. 1 [Fig. 2(a)] with the same portion of the simulated absorption spectrum [i.e., the low excitation energy part; Fig. 2(b)] and bearing in mind that the LIF spectrum has not been corrected for laser intensities of the two dyes used, the agreement between theory and experiment can be considered as reasonably good. In particular, the simulated and observed spectra show the very similar doublet feature mentioned above. The agreement of the observed LIF spectrum in this respect is especially good in the 350–380 nm region with the simulated spectrum which does not include hot bands [Fig. 1(b)]. However, on including hot bands, as shown in Fig. 2(b), the weak vibrational feature in the simulated spectrum underneath the main doublet structure appears to be too strong/congested c.f. the observed LIF spectrum in this spectral region. The latter appears to be pretty clean with mainly the doublet structure mentioned above and very little weak structure underneath the major doublet structure. We will come back to this point later. Considering the 380–405 nm region in detail [see the inset in Fig. 2(b) and particularly Fig. 3], the match between the simulated and observed spectra is very good including the weak structure from the hot bands. This supports strongly the vibrational assignment of Hullah and Brown[1] and their position of the (0-0) band. Lastly, we just note that from the computed FCFs, the $(1)^1B_2(1,m,0) \leftarrow \tilde{\mathbf{X}}\,^1A_1(1,1,0)$ hot band series overlaps with the main $(1)^1B_2(0,n,0) \leftarrow \tilde{\mathbf{X}}\,^1A_1(0,0,0)$ series (vibrational components of the two series with $m=n+2$ differ by ca. 3 cm^{-1}; see Fig. 3), though the contribution from the hot band series is very small.

TABLE VII. Vibrational populations of low-lying vibrational levels of the $\tilde{\mathbf{X}}\,^1A_1$ state employed to simulate the hot bands of the $(1)^1B_2 \leftarrow \tilde{\mathbf{X}}^1A_1$ absorption spectrum of TeO_2.

$\tilde{\mathbf{X}}\,^1A_1(v_1,v_2,v_3)$	Relative population
(0,0,0)	1.000 000
(0,1,0)	0.126 189
(0,2,0)	0.015 951
(1,0,0)	0.032 880
(0,3,0)	0.002 020
(1,1,0)	0.005 592
(0,4,0)	0.000256

IV. CONCLUDING REMARKS

Summarizing, comparison between simulated $(1)^1B_2 \leftarrow \tilde{\mathbf{X}}\,^1A_1$ absorption and observed LIF spectra leads to the following conclusion. First, despite the lack of dye laser intensity correction in the LIF spectrum, it can be concluded that our spectral simulation confirms the assignments of Hullah and Brown[1] on the molecular carrier of, electronic states involved in, and vibrational structure of their observed LIF spectrum. Second, our spectral simulation suggests that the reported LIF spectrum is only part of the full absorption spectrum, which should extend to higher excitation energy than the spectrum presented in Ref. 1. Third, the higher excitation energy region of the LIF spectrum (from 345 to ca. 375 nm) appears to be less congested than the lower excitation energy region of 380–400 nm [see Fig. 2(a)]. Our spectral simulation suggests that the higher energy region of the LIF spectrum is ''cooler'' than the lower energy region. This leads to the suggestion that the experimental conditions used to record the two dye regions in Ref. 1, shown in Figure 1(a), are probably not the same. It appears that the portion of the LIF spectrum recorded using the higher energy dye, DMQ, was obtained from a gas-phase sample at a lower vibrational

temperature than that used to record the lower energy region with the dye, BBQ. Fourth, for the lower excitation energy region of the LIF spectrum, spectral simulation suggests a non-Boltzmann population distribution in the low-lying vibrational levels of the $\tilde{\mathbf{X}}\,^1A_1$ state. However, it appears that only the vibrational populations of the $\tilde{\mathbf{X}}(1,0,0)$ and (1,1,0) levels deviate significantly from a Boltzmann distribution at 200 K, suggesting that on vaporization of solid TeO_2 at ca. 1123 K in an alumina tube and expansion through a 250 μm hole with a ca. 2.5 bar of argon backing pressure,[1] vibrational deactivation of the population in the (1,0,0) and (1,1,0) levels of the $\tilde{\mathbf{X}}\,^1A_1$ state of TeO_2 is a lot less efficient than for the other vibrational levels, for example, the (0,1,0) and (0,2,0) levels.

In conclusion, we have reported near state-of-the-art *ab initio* calculations and reliable Franck-Condon simulations, which have contributed much to the understanding of the low-lying electronic states of TeO_2 and its observed LIF spectrum.[1] Based on the results of the *ab initio* calculations and comparison between the simulated $(1)^1B_2 \leftarrow \tilde{\mathbf{X}}\,^1A_1$ absorption spectrum and the experimental LIF spectrum, the recommended geometries for the electronic states involved are $r_e = 1.7851$ Å, $\theta_e = 111.36°$ for the $\tilde{\mathbf{X}}\,^1A_1$ state and $r_e = 1.8786$ Å, $\theta_e = 100.1°$ for the $(1)^1B_2$ state.

ACKNOWLEDGMENTS

The authors are grateful to the Research Grant Council (RGC) of the Hong Kong Special Administrative Region (HKSAR, Grant Nos. AoE/B-10/1 and PolyU 5003/03P) and the Research Committee of the Hong Kong Polytechnic University, HKSAR (Grant No. G-T635) for financial support. The EPSRC (UK) National Service for Computational Chemistry Software is acknowledged for providing computational resources in carrying out the *ab initio* calculations of this study. This work was also supported by the Leverhulme Trust. Helpful discussion with Professor J. M. Brown (Oxford) is also gratefully acknowledged.

[1] D. F. Hullah and J. M. Brown, J. Mol. Spectrosc. **200**, 261 (2000).
[2] G. W. King and P. R. McLean, J. Mol. Spectrosc. **51**, 363 (1974).
[3] A. Stromberg, O. Gropen, and U. Wahlgren, J. Chem. Phys. **80**, 1593 (1984).
[4] A. Stromberg, U. Wahlgren, and O. Lindqrist, Chem. Phys. **100**, 229 (1985).
[5] J. Janszky, R. H. Bartram, A. R. Rossi, and G. Corradi, Chem. Phys. Lett. **124**, 26 (1986).
[6] H. Basch, D. Cohen, and M. Albeck, Chem. Phys. Lett. **144**, 450 (1988).
[7] R. J. M. Konings, A. S. Booij, and A. Kovacs, Chem. Phys. Lett. **292**, 447 (1998).
[8] A. V. Marenich and V. G. Solomonik, J. Phys. Chem. **73**, 1993 (1999).
[9] E. P. F. Lee, D. K. W. Mok, J. M. Dyke, and F.-T. Chau, Chem. Phys. Lett. **340**, 348 (2001).
[10] D. K. W. Mok, E. P. F. Lee, F.-T. Chau, and J. M. Dyke, J. Comput. Chem. **22**, 1896 (2001).
[11] E. P. F. Lee, J. M. Dyke, D. K. W. Mok, R. P. Claridge, and F.-T. Chau, J. Phys. Chem. A **105**, 9533 (2001).
[12] E. P. F. Lee, D. K. W. Mok, J. M. Dyke, and F.-T. Chau, J. Phys. Chem. A **106**, 10130 (2002).
[13] P. J. Hay and W. R. Wadt, J. Chem. Phys. **82**, 270 (1985).
[14] Pseudopotentials of the Stuttgart/Koeln group (Revision: February 7, 2003): Hermann Stoll (stoll@theochem.uni-stuttgart.de) or Michael Dolg (dolg@thch.uni-bonn.de or m.dolg@uni-koeln.de).
[15] J. M. L. Martin and A. Sundermann, J. Chem. Phys. **114**, 3408 (2001).
[16] R. A. Kendall, T. H. Dunning, Jr., and R. J. Harrison, J. Chem. Phys. **96**, 6796 (1992).
[17] M. J. Frisch, G. W. Trucks, H. B. Schlegel *et al.*, Gaussian 03, Revision B.01, (Gaussian, Inc., Pittsburgh, PA, 2003).
[18] T. H. Dunning, Jr., J. Chem. Phys. **90**, 1007 (1989), D. E. Woon and T. H. Dunning, Jr., *ibid.* **103**, 4572 (1995).
[19] MOLPRO is a package of *ab initio* programs written by H.-J. Werner and P. J. Knowles, with contributions from J. Almlöf, R. D. Amos, A. Berning *et al.*
[20] N. Godbout, D. R. Salahub, J. Andzelm, and E. Wimmer, Can. J. Chem. **70**, 560 (1992).
[21] S. Carter and N. C. Handy, J. Chem. Phys. **87**, 4294 (1987).
[22] J. E. Dennis, Jr., D. M. Gay, and R. E. Welsh, ACM Trans. Math. Softw. **7**, 348 (1981).
[23] J. K. G. Watson, Mol. Phys. **19**, 465 (1970).
[24] D. W. K. Mok, E. P. F. Lee, F.-T. Chau, D.-C. Wang, and J. M. Dyke, J. Chem. Phys. **113**, 5791 (2000).
[25] F.-T. Chau, J. M. Dyke, E. P. F. Lee, and D. K. W. Mok, J. Chem. Phys. **115**, 5816 (2001).
[26] E. Z. Zasorin, J. M. Zharskii, G. F. Pinaev, V. N. Kupreev, and V. P. Spiridonov, Russ. J. Struct. Chem. **15**, 588 (1974).
[27] D. W. Muenow, J. W. Hastie, R. Hauge, R. Bautista, and J. L. Margrave, Trans. Faraday Soc. **65**, 3210 (1969).
[28] A. J. Hinchcliffe, PhD thesis, University of Oxford, 1971.
[29] M. Spoliti, S. Nunziante Cesaro, and E. Coffari, J. Chem. Thermodyn. **4**, 507 (1972).
[30] R. Migeotte, Ph.D. thesis, Leige, 1941.
[31] I. Dubois, Bull. Soc. Sci. Liege **1–2**, 63 (1970).